batteries

MDPI

Article

Lipoic Acid-Derived Interphase for Stable Lithium Metal Anodes in High-Performance Lithium Metal Batteries

Liyuan Zhang [1,*], Chen Liang [1], Jiarong Xu [2], Chuanhui Gong [2,*] and Wei Chen [3,*]

[1] School of Marxism, Central University of Finance and Economics, Beijing 100081, China
[2] Guangdong Greater Bay Area Institute of Aerospace Information, Guangzhou 510000, China
[3] State Key Laboratory of Electronic Thin Films and Integrated Devices, University of Electronic Science and Technology of China, Chengdu 610054, China
* Correspondence: zhangliyuan@cufe.edu.cn (L.Z.); gongch@aircas.ac.cn (C.G.); weichen@uestc.edu.cn (W.C.)

Abstract

Lithium metal batteries are widely regarded as one of the most promising candidates for achieving energy densities beyond 500 Wh kg^{-1}. However, their practical commercialization is severely hindered by the high reactivity of lithium metal, which leads to pronounced interfacial instability. Constructing an artificial solid electrolyte interphase (SEI) via surface pretreatment has been demonstrated to be an effective strategy for suppressing dendrite growth and mitigating parasitic side reactions. Herein, we take advantage of the rapid reaction between lipoic acid (LA) and lithium metal to pre-form a uniform artificial SEI on the anode surface. This interphase is composed of organic COO-Li species and sulfur-containing compounds. Electrochemically, the LA-modified lithium anode exhibits remarkable stability, sustaining more than 1500 h of cycling in symmetric cells at 5 mA cm^{-2} and 5 mAh cm^{-2}. Furthermore, full-cell configurations, including lithium-sulfur and lithium-$LiFePO_4$ pouch cells, deliver significantly improved cycling performance compared with those employing bare lithium anodes. These results establish a practical and scalable route for fabricating stable artificial SEI layers on lithium metal, thereby providing a feasible pathway toward the realization of high-energy-density lithium metal batteries.

Keywords: solid electrolyte interphase; artificial SEI layers; lithium metal anode; full-cell configurations; lithium sulfur batteries

1. Introduction

Lithium metal, with its ultrahigh theoretical capacity (3860 mAh g^{-1}) and low electrochemical potential (−3.04 V vs. SHE), is often considered the "holy grail" of anode materials for next-generation high-energy-density batteries [1,2]. These intrinsic properties position lithium as a prime candidate for enabling advanced storage systems [3,4], such as lithium-sulfur and lithium-iron phosphate batteries, that could meet escalating energy demands from electric vehicles and grid storage [5]. However, the practical implementation of lithium metal anodes has been fundamentally constrained by persistent interfacial challenges. Uncontrolled dendrite growth, persistent parasitic reactions, and an inherently unstable solid-electrolyte interphase (SEI) contribute not only to rapid capacity fade and poor Coulombic efficiency [6,7], but also to serious safety risks, including internal short circuits that collectively impede the commercialization of lithium metal batteries [8,9].

The solid-electrolyte interphase (SEI) plays a decisive role in regulating lithium deposition and maintaining long-term interfacial stability [10,11]. Recent artificial-SEI strategies

Check for updates

Academic Editor: Yong-Joon Park

Received: 22 June 2026
Revised: 31 July 2026
Accepted: 5 August 2026
Published: 14 August 2026

Copyright: © 2026 by the authors. Licensee MDPI, Basel, Switzerland. This article is an open access article distributed under the terms and conditions of the Creative Commons Attribution (CC BY) license.

for lithium-metal anodes, including solution-processed inorganic layers [12], in situ chemically converted interphases [13], polymeric coatings [14], and organic–inorganic hybrid layers [15], have increasingly demonstrated that stabilizing Li metal requires not only the mechanical suppression of dendrite growth but also precise regulation of interphase chemistry and Li^+ transport kinetics. For instance, Cao et al. introduced a multifunctional electrolyte additive that promoted the formation of uniform LiF-, Li_3N-, and LiBOx-rich interphases on both the Li-metal anode and the LiFePO4 cathode [16], underscoring the importance of constructing compositionally uniform, ionically conductive, and chemically robust interphases to achieve highly reversible Li plating and stripping [17]. Hu et al. demonstrated that an in situ formed Li_3Sb alloy layer could raise the surface Young's modulus and thereby suppress dendritic growth during cycling [18,19]. Nevertheless, existing artificial interphases often require compromises among Li^+ transport, mechanical robustness, interfacial adhesion, chemical stability, and fabrication complexity [20–22]. Developing a simple and scalable solution-based surface treatment that enables the formation of a uniform organic–inorganic interphase while preserving efficient Li^+ transport and long-term interfacial stability remains highly desirable.

In this work, we develop a simple, low-cost, and readily scalable surface-modification strategy for Li-metal anodes using a lipoic acid (LA) solution. This treatment forms a uniform organic–inorganic hybrid interphase on the Li surface. At a sulfur loading of 3 mg cm^{-2}, the LA-modified Li–S cell maintains a specific capacity of approximately 1000 mAh g^{-1} over 70 cycles. The LA-modified $LiFePO_4$ cell also exhibits stable cycling for more than 200 cycles, significantly outperforming the cell using a pristine Li anode. These results demonstrate that LA treatment is an effective and rapid approach for stabilizing Li-metal anodes. By facilitating Li^+ transport and enhancing interfacial stability, the resulting hybrid interphase improves the cycling performance of Li-metal batteries. The simplicity and scalability of this strategy further highlight its potential for practical high-capacity Li-metal cells.

2. Experimental Section

Lithium foil modification. A 50 μm-thick lithium metal foil (99.9% purity, Shengxin Lithium Energy Co., Ltd., Chengdu, China) was mechanically polished to remove surface oxides, subsequently washed in anhydrous tetrahydrofuran for 10 min, and then dried in an argon-filled glovebox (H_2O and O_2 levels < 0.1 ppm). A homogeneous 0.1 M solution was prepared by dissolving lipoic acid (LA, purity ≥ 99%, Aladdin) in anhydrous tetrahydrofuran inside the same glovebox. The pretreated lithium foil was immersed completely in the LA solution for 5 min to form a thin sulfur-based composite layer. After reaction, the foil was rinsed thoroughly with anhydrous tetrahydrofuran to remove any unreacted LA and dried under vacuum (40 °C, $<10^{-3}$ mbar) for 2 h inside the glovebox.

Electrode Preparation. Sulfur cathodes were fabricated as follows. Commercial sulfur powder and acetylene black were first mixed at a mass ratio of 7:3 and subjected to ball-milling at 300 rpm for 2 h. The resulting sulfur/carbon composite was then heated in a sealed reactor at 155 °C for 12 h and allowed to cool to room temperature. The composite was subsequently mixed with Ketjen black and poly (vinylidene fluoride) (PVDF) at a mass ratio of 8:1:1 in N-methyl-2-pyrrolidone (NMP) and stirred for 24 h to obtain a homogeneous slurry. The slurry was uniformly coated onto carbon-coated aluminum foil and dried under vacuum to yield the sulfur electrode. For the lithium iron phosphate ($LiFePO_4$) cathode, a slurry was prepared by dispersing $LiFePO_4$ powder, PVDF and conductive carbon black in NMP at a mass ratio of 9:0.5:0.5, which was then coated onto carbon-coated aluminum foil and dried to form the $LiFePO_4$ electrode. For the Li–S pouch cells, the active electrode area was 10 cm^2, the sulfur loading was 3 mg cm^{-2}, and the total electrolyte amount was 240 μL,

corresponding to an E/S ratio of 8 μL mg^{-1}. The Li-metal thickness and dimensions were 50 μm, respectively, giving an N/P ratio of ~2, calculated on the basis of the theoretical areal capacity of lithium and the sulfur cathode capacity. For the Li–$LiFePO_4$ pouch cells, the active cathode area was 10 cm^2, the $LiFePO_4$ loading was 3 mg cm^{-2}, and the electrolyte amount was 200 μL. The Li-metal thickness and area were 50 μm and 10 cm^2, respectively. The pouch cells had external dimensions of 3 × 4 cm^2 and an effective electrode area of 10 cm^2. And the loading of cathode materials is 3 mg cm^{-2}.

Electrochemical Characterization. Symmetric Li | Li cells were assembled using the modified lithium foil (14 mm diameter) with an electrolyte of 1 M LiTFSI in a 1:1 (*v*/*v*) mixture of 1,3-dioxolane (DOL) and 1,2-dimethoxyethane (DME), containing 2 wt% $LiNO_3$. Symmetric cells were assembled using coin cell cases with two pristine Li or LA-Li electrodes (14 mm in diameter) and a PP (Celgard 2400, 6 μm thick). Galvanostatic cycling tests were performed to assess the uniformity of lithium deposition and stripping. In addition, lithium-sulfur (Li–S) and lithium iron phosphate ($LiFePO_4$) full cells were fabricated in an argon-filled glovebox following the procedures described above for further electrochemical evaluation. Unless otherwise specified, three independently assembled cells were tested for each sample (n = 3).

Interfacial Characterization. The surface morphology of the lithium foils before and after modification was examined by scanning electron microscopy (SEM, Quanta 200, FEI Company, Hillsboro, OR, USA). The chemical composition of the resulting solid-electrolyte interphase (SEI) was analyzed using X-ray photoelectron spectroscopy (AXIS Supra, Kratos Analytical Ltd., Manchester, UK.), with particular attention paid to the S 2p and F 1s spectral regions. Survey and high-resolution spectra were acquired at pass energies of 150 eV and 25 eV, respectively. To evaluate the stability of the electrode-electrolyte interface, electrochemical impedance spectroscopy (EIS) measurements were performed. For the XPS measurements shown in Figure 5, the cells were cycled at 10 mA cm^{-2} and 1 mAh cm^{-2} for 10 cycles. The cells were disassembled in an Ar-filled glovebox. The collected Li electrodes were washed with DOL solution for three times, dried in the glovebox, and transferred to the XPS instrument using an airtight transfer vessel without air exposure.

3. Results and Discussion

The interfacial modification of the lithium anode using lipoic acid (LA) is illustrated in Figure 1a. Initially, the carboxylic acid group of LA reacts with metallic Li to form lithium carboxylate species with concurrent H_2 evolution. Meanwhile, electron transfer from Li promotes partial reductive cleavage of the strained S–S bond, producing surface-bound lithium thiolate species. Further reduction near the Li surface may generate more highly lithiated sulfur species. The resulting interphase is therefore proposed to be a compositionally graded organic–inorganic layer containing COO–Li, residual S–S bonds, lithium thiolates or polysulfide-like species, and other Li–S components. In addition, THF may participate in the formation of a native passivation layer on the highly reducing Li surface, involving trace proton-containing species that may produce lithium alkoxides, Li_2O, and possibly LiH. The surface morphologies of the pristine and modified Li anodes are shown in Figure 1b,c. Compared with the microscopically rough pristine Li surface, the LA-treated anode exhibits a more uniform and continuous morphology, indicating successful surface modification. This interfacial layer may promote more homogeneous Li ion transport and deposition. To optimize its thickness, Li foils were treated under identical conditions while varying only the reaction time, which is a key parameter affecting the layer thickness and electrochemical performance.

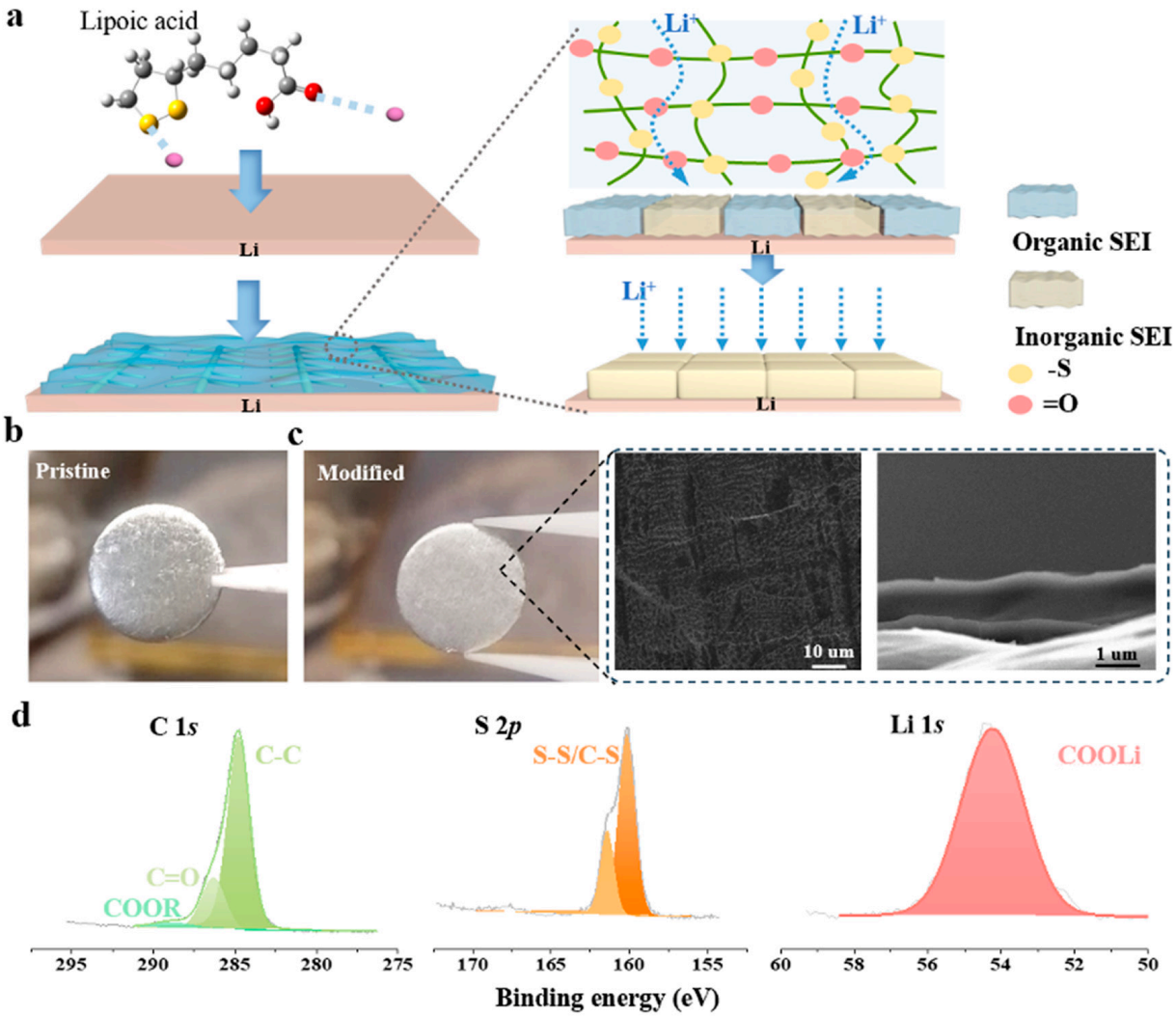

Figure 1. Designing concept of LA-Li. (**a**) Design a schematic diagram showing that lipoic acid (LA) directly reacts with lithium (Li) to form an organic-inorganic composite artificial solid electrolyte interphase (SEI) on the lithium surface. (**b**,**c**) Optical photographs of pristine Li and modified Li. Scanning Electron Microscopy (SEM) images are inserted, in which an artificial SEI thickness of approximately 1 μm can be clearly observed. (**d**) X-ray Photoelectron Spectroscopy (XPS) information of the LA-Li surface.

To clarify the chemical composition of the modified Li surface, the interphase was analyzed by X-ray photoelectron spectroscopy (XPS, Figure 1d). The C 1s spectrum shows C–C, C=O, and carboxylate-related components, indicating the presence of organic species. The S 2p spectrum contains residual S–S and reduced Li–S species, consistent with the incorporation and partial reductive conversion of LA-derived sulfur groups. The Li 1s spectrum further supports the formation of lithium carboxylate species. Collectively, these results indicate the formation of an organic–inorganic hybrid interphase, consistent with the proposed mechanism in Figure 1a. Combined with the morphological results, this interphase is expected to promote more uniform Li^+ transport and deposition, thereby improving interfacial stability and suppressing dendritic Li growth [23,24].

To assess the interfacial stability of the lithium metal anode, symmetric cells were cycled to evaluate the performance of the lipoic acid (LA)-constructed artificial SEI. As shown in Figure 2a, long-term voltage–time profiles (0–1500 h) for symmetric Li||Li cells cycled under 5 mA cm^{-2} and 5 mAh cm^{-2} have been provided. The LA-modified cell exhibits a stable voltage plateau near 0.1 V with negligible fluctuation, reflecting a highly

stable interface during repeated plating/stripping and effective suppression of dendrite growth and parasitic reactions. In contrast, the pristine Li cell fails to sustain long-term cycling stability, with its voltage profile becoming irregular shortly after cycling begins. As seen in the magnified view (Figure 2b), the LA-modified cell maintains minimal polarization and steady voltage traces, whereas the pristine cell displays severe voltage oscillations, with extremes dipping to around −0.3 V. These oscillations point to substantial interfacial impedance variation and poor deposition uniformity in the unmodified electrode, where uncontrolled dendritic growth leads to rapid interfacial degradation. Figure 2c compares the long-term cycling behavior of LA-Li and pristine Li symmetric cells at 10 mA cm^{-2} and 1 mAh cm^{-2}. During the initial cycling stage, the pristine Li cell exhibits relatively large and unstable polarization, reflecting heterogeneous Li deposition and continuous interfacial degradation. At the later stage, however, its apparent voltage decreases to an abnormally low level, as highlighted in Figure 2d, most likely resulting from dendritic Li-induced soft short circuit. In contrast, the LA-Li cell retains clear and periodically reversible voltage profiles throughout prolonged cycling, demonstrating sustained Li plating/stripping without catastrophic short circuit.

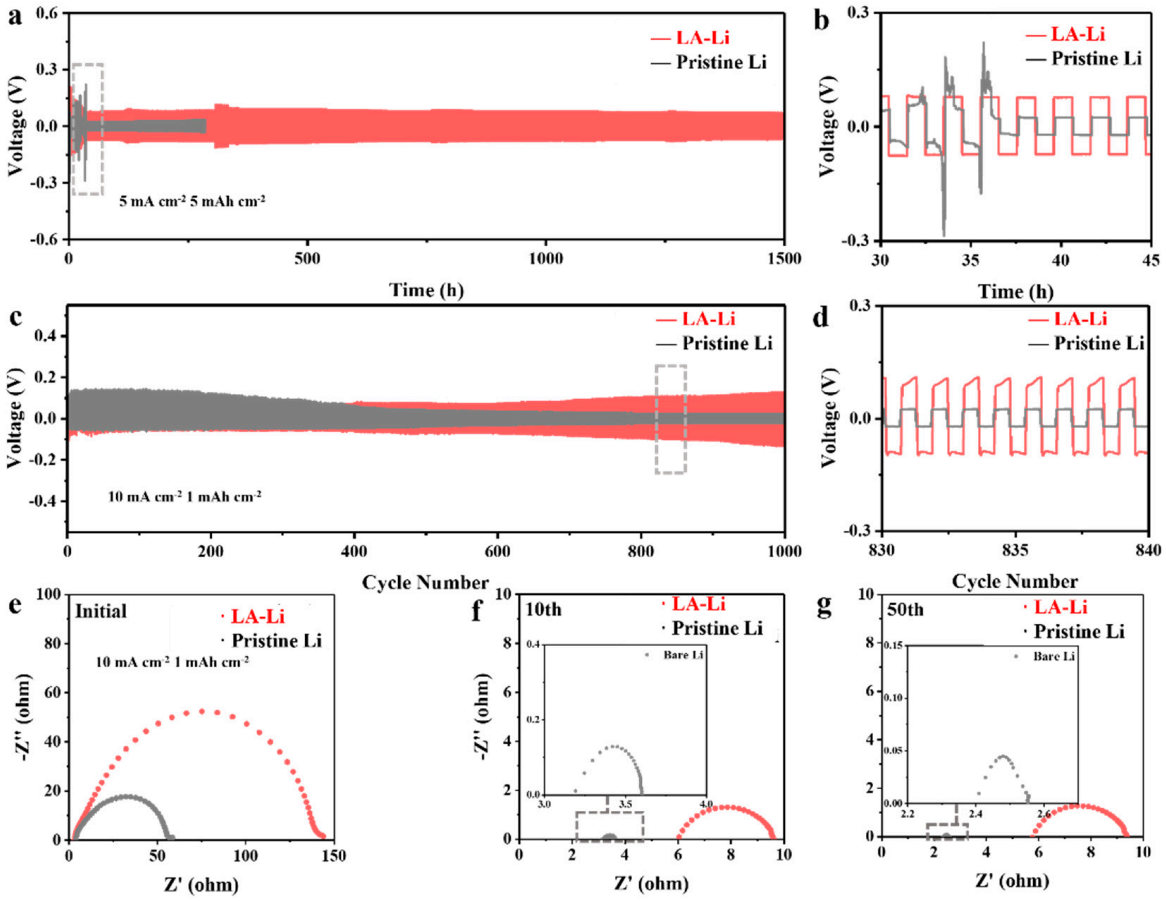

Figure 2. The characterization of interfacial stability. (**a**) Cycling stability of lithium symmetric batteries under high current density (5 mA cm^{-2}) and high capacity (5 mAh cm^{-2}) conditions. (**b**) Partial magnification image. (**c**) Cycling stability of lithium symmetric batteries under high current density (10 mA cm^{-2}) with a capacity of 1 mAh cm^{-2}. (**d**) Partial magnification image. (**e**–**g**) Interfacial impedance spectra (EIS) of lithium symmetric batteries at different cycle numbers.

Interfacial impedance evolution is shown in Figure 2e–g. Electrochemical impedance spectroscopy (EIS) was first measured before cycling to evaluate the initial interfacial ion-transport characteristics (Figure 2e). At this stage, the LA-modified cell exhibits a higher

interfacial charge-transfer resistance (R_{ct}) than the pristine cell, which we attribute to the presence of a composite interphase comprising organic constituents along with inorganic species. Upon cycling, however, the interface undergoes progressive stabilization. As shown in Figure 2f,g, the R_{ct} of the LA-modified cell remains nearly invariant after the 10th and 50th cycle, indicating exceptional interfacial durability. In contrast, reliable R_{ct} values for the pristine cell could not be consistently obtained in later cycles, likely owing to internal micro-short circuits induced by dendritic growth, thus confirming the effectiveness of our strategy under high-current-density operation.

Figure 3 presents the scanning electron microscopy (SEM) images of lithium metal electrodes at 10 mA cm^{-2}, comparing both top-view and cross-sectional morphologies to systematically evaluate the influence of surface modification on lithium deposition. After 10 cycles, the pristine Li electrode exhibits an irregular, cluster-like surface (Figure 3a), indicative of heterogeneous deposition and dendritic growth. By contrast, the LA-modified electrode displays a dense and uniform granular structure (Figure 3b), with no visible dendritic features, demonstrating markedly more homogeneous and regulated lithium plating.

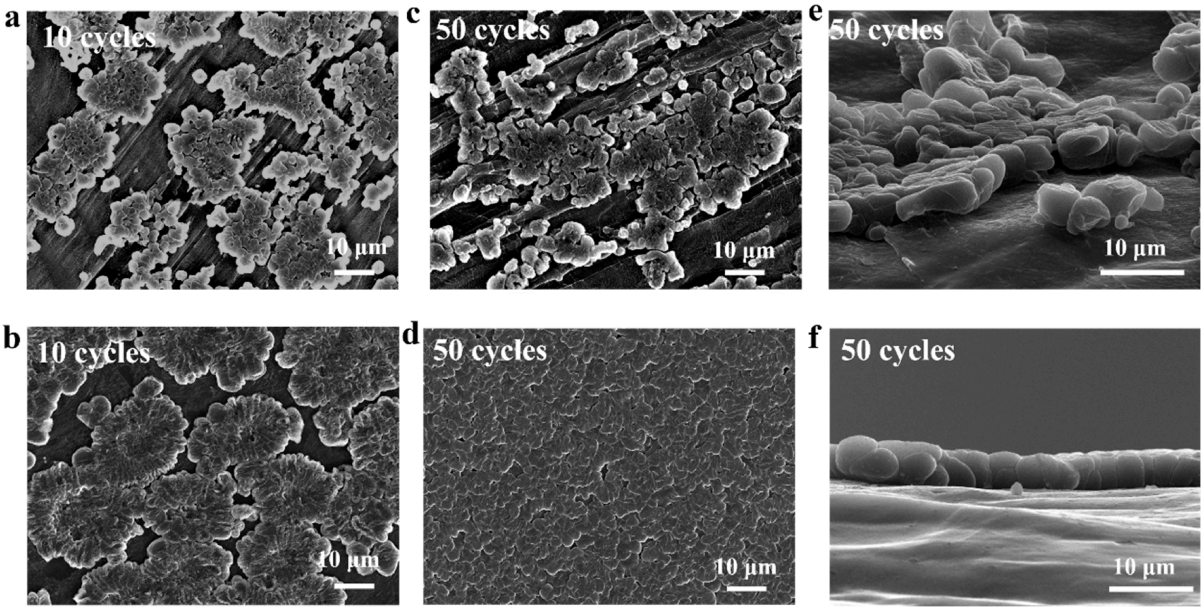

Figure 3. Scanning Electron Microscopy (SEM) images at 10 mA cm^{-2} and 1 mAh cm^{-2}. (**a**,**b**) SEM images of pristine Li (**a**) and LA-Li (**b**) after the 10th cycle. (**c**,**d**) SEM images of pristine Li (**c**) and LA-Li (**d**) after the 50th cycle. (**e**,**f**) Cross-sectional SEM images of pristine Li (**e**) and LA-Li (**f**) after the 50th cycle.

By the 50th cycle, the pristine Li electrode develops increasingly heterogeneous and disordered deposits (Figure 3c). In contrast, the LA-modified electrode retains a compact and uniform granular morphology without pronounced dendritic growth (Figure 3d), indicating more stable Li deposition during prolonged cycling. Cross-sectional images further reveal a rough, uneven deposition layer with prominent dendritic protrusions on pristine Li (Figure 3e), which may cause local stress concentration and increase the risk of separator penetration. Conversely, the LA-modified electrode displays a smooth and continuous deposition layer with uniform thickness and no dendritic features (Figure 3f).

To further evaluate the effectiveness and practical potential of our approach, we assembled and tested pouch-type full cells. As shown in Figure 4a, the electrochemical performance was systematically characterized in both lithium-sulfur (Li-S) and lithium-$LiFePO_4$ (Li-LFP) configurations. In the Li-S system (Figure 4b,c) cycled at 0.3 C with a sulfur loading of 3 mg cm^{-2}, the cell equipped with the LA-modified anode (LA-Li–

S) displays markedly improved capacity retention compared to its counterpart with a pristine Li anode (pristine Li–S). The slower capacity fading observed in the LA-Li–S cell suggests that the modified interface effectively alleviates degradation caused by polysulfide shuttling and lithium dendrite growth. Corresponding voltage–capacity profiles at selected cycles (Figure 4c) further show that the LA-Li–S cell maintains more stable voltage plateaus and reduced polarization, whereas the pristine cell exhibits noticeable voltage decay.

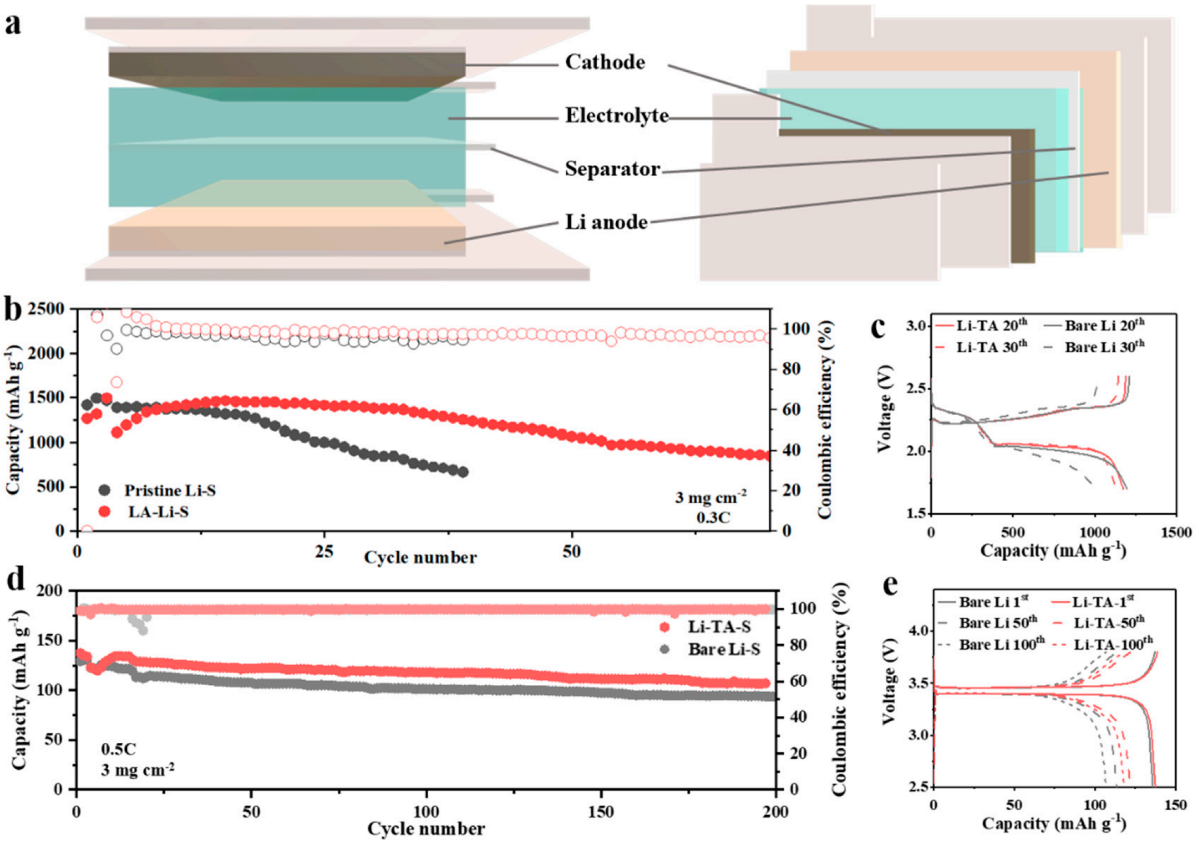

Figure 4. Electrochemical performance analysis of pouch batteries. (**a**) Schematic diagram of pouch cell structure. (**b**) Cycling data of lithium-sulfur batteries at a rate of 0.3 C with a sulfur loading of 3 mg cm^{-2}. (**c**) Charge–discharge curves of lithium-sulfur batteries (voltage range: 1.6–2.8 V). (**d**) Cycling data of lithium iron phosphate (LFP) pouch cells at a rate of 0.5 C with an LFP loading of 3 mg cm^{-2}. (**e**) Charge–discharge curves at different cycle numbers.

In the Li–LFP system (Figure 4d,e), cycled at 0.5 C with an electrode loading of 3 mg cm^{-2}, the LA-Li–LFP cell delivers an initial discharge capacity of approximately 135 mAh g^{-1} and exhibits gradual capacity fading after the initial activation period. Its capacity decreases to 80% of the initial value after 180 cycles. In comparison, the pristine Li–LFP cell reaches 80% of its initial capacity after approximately 80 cycles, indicating substantially faster degradation. The voltage–capacity profiles (Figure 4e) show that the LA-modified cell retains distinct voltage plateaus with lower polarization at high rates, indicating improved rate capability. This enhancement is attributed to the combined passivation and deposition-regulation effects of the LA-derived interphase.

Figure 5 reveals the depth-dependent interphase chemistry and structural role of LA-Li through S 2p, F 1s, and C 1s XPS spectra collected before and after Ar^+ sputtering. In the S 2p spectra (Figure 5a), the LA-Li system contains Li–S species, S–C/S–S environments, and oxidized sulfur products across different depths, indicating a chemically graded interphase. Without LA-Li, the interphase is mainly dominated by Li–S species, with limited oxidized sulfur components. This confirms that LA-Li regulates sulfur-containing

electrolyte decomposition and promotes a more diverse interphase composition. The F 1s spectra (Figure 5b) show that the LA-Li system contains both LiF and CF_x species, with LiF remaining in the inner region after sputtering. This suggests a layered interphase with an organic-rich outer layer and a LiF-rich inner layer. In contrast, the LA-free interphase is largely dominated by LiF. The hybrid structure formed with LA-Li better combines mechanical strength, interfacial flexibility, and ion transport. The C 1s spectra (Figure 5c) further identify C–C, C–O, carboxylate, and CF_x species, confirming the formation of an organic–inorganic hybrid interphase. The organic components improve interfacial compliance, while the inorganic LiF-rich phase enhances mechanical stability and suppresses continuous electrolyte decomposition. As illustrated in Figure 5d, the depth-profile XPS results indicate that LA participates in the formation of a sulfur- and oxygen-containing interphase on the Li-metal surface. The coexistence of S–S/C–S and Li–S species is consistent with partial reductive cleavage or lithiation of the disulfide moiety, producing surface-bound reduced sulfur species while retaining a fraction of the original disulfide-containing structures. Meanwhile, the formation of LiF and salt-derived sulfur-containing species indicates that electrolyte decomposition also contributes to the interphase. Therefore, the resulting SEI is proposed to be an organic–inorganic hybrid layer containing reduced sulfur species, LiF, and oxygen-containing organic components.

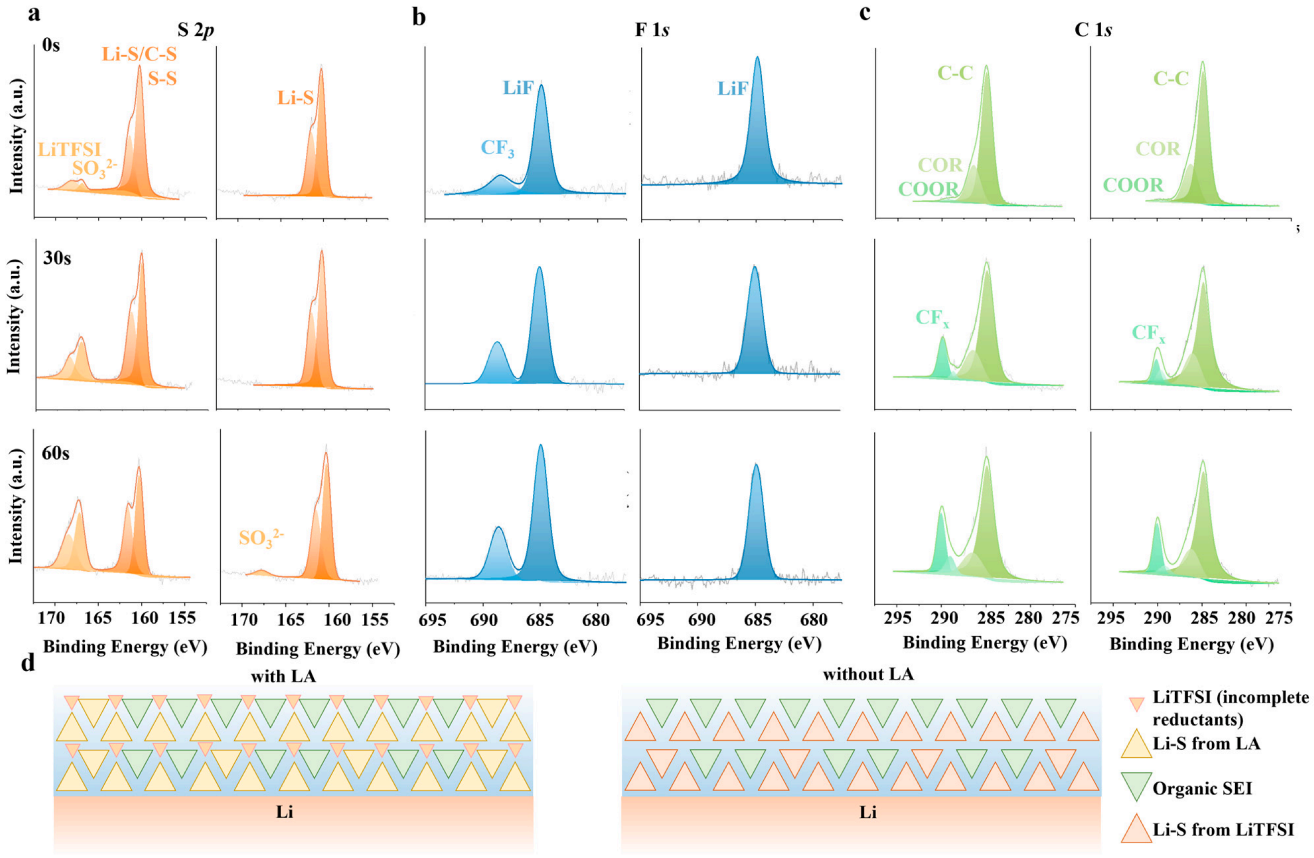

Figure 5. Depth-dependent interphase chemistry and the role of LA-Li. Depth-resolved XPS spectra of (**a**) S 2p, (**b**) F 1s, and (**c**) C 1s after 0, 30, and 60 s of sputtering. (**d**) Schematic illustration showing that LA-derived Li^+ compensates for incomplete LiTFSI coordination sites, improves structural continuity, and stabilizes the interface. This dual Li^+-compensation and interphase-regulation effect enables uniform ion transport, enhanced mechanical stability, and suppressed side reactions.

4. Conclusions

In summary, a rapid 5 min ex situ LA treatment forms a preconstructed interphase on Li metal with minimal Li consumption. Surface and depth-profile XPS analyses indicate partial conversion of the disulfide and carboxylic acid groups, producing an S/O-containing organic–inorganic interphase. These results support the role of LA as a multifunctional molecular precursor rather than a simple physical coating. As a result, the LA-modified Li electrode enables compact Li deposition, stable interfacial impedance, and symmetric-cell cycling for over 1500 h at 5 mA cm^{-2} and 5 mAh cm^{-2}. Enhanced capacity retention and Coulombic efficiency in both Li–S and Li–$LiFePO_4$ pouch-type cells further demonstrate its applicability across different cathode chemistries. These results establish molecularly programmed surface conversion as a simple and efficient strategy for stabilizing reactive Li interfaces and highlight the integration of complementary functional groups within small molecules as a general design principle for artificial interphases.

Author Contributions: Conceptualization, L.Z. and W.C.; methodology, C.L.; validation, J.X. and C.G.; formal analysis, C.G.; investigation, L.Z.; writing—original draft preparation, W.C.; writing—review and editing, C.G.; visualization, W.C.; supervision. All authors have read and agreed to the published version of the manuscript.

Funding: This research received no external funding.

Data Availability Statement: The original contributions presented in this study are included in the article. Further inquiries can be directed to the corresponding authors.

Conflicts of Interest: The authors declare no conflicts of interest.

References

1. Chen, D.; Chen, W.; Zhang, B.; Hu, Y.; Wang, S.; Lei, T.; He, M.; Fan, Y.; Zhou, M.; Yan, Y.; et al. High Partial Molar Volume Polymer Electrolyte for Upgraded Lithium Metal Batteries. *Angew. Chem. Int. Ed.* **2025**, *64*, e202500896. [CrossRef] [PubMed]
2. Ryu, M.; Park, S.O.; Lim, S.; Lee, H.; Lee, J.H.; Lee, G.; Bae, K.Y.; Kim, J.Y.; Kong, Y.; Son, S.; et al. Low-strain metal–organic framework negative electrode for stable all-solid-state batteries. *Nat. Commun.* **2025**, *16*, 9722. [CrossRef] [PubMed]
3. Mao, S.; Wang, Y.; Lu, Y.; Han, X.; Zheng, Y.; Feng, X.; Ren, X.; Lu, L.; Ouyang, M. In situ evaluation and manipulation of lithium plating morphology enabling safe and long-life lithium-ion batteries. *InfoMat* **2025**, *7*, e12612. [CrossRef]
4. Liu, S.; He, M.; Wang, S.; Hu, Y.; Chen, D.; Shu, C.; Lv, W.; Chen, B.; Chen, D.; Xia, L.; et al. Design of lithium metal−compatible sulfide electrolytes by electronic structure engineering for all−solid−state lithium metal batteries. *Nano Energy* **2025**, *142*, 111176. [CrossRef]
5. Zhu, X.; Iqbal, S.; Kumar, N.; Liu, H.; Dou, S.; Wang, N.; Bai, Z. The catalytic chemistry for high-performance lithium–sulfur batteries: A review and prospects. *Adv. Funct. Mater.* **2025**, *35*, e11659. [CrossRef]
6. Chen, W.; Hu, Y.; Lv, W.; Lei, T.; Wang, X.; Li, Z.; Zhang, M.; Huang, J.; Du, X.; Yan, Y.; et al. Lithiophilic montmorillonite serves as lithium ion reservoir to facilitate uniform lithium deposition. *Nat. Commun.* **2019**, *10*, 4973. [CrossRef] [PubMed]
7. Zhou, C.; Guo, W.; Fan, J.; Shi, N.; Zhao, Y.; Yang, X.; Ding, Z.; Han, M.; Huang, W. Recent advances and future perspectives of Ruddlesden–Popper perovskite oxides electrolytes for all-solid-state batteries. *InfoMat* **2024**, *6*, e12563. [CrossRef]
8. Zhao, M.; Zhang, J.; Costa, C.M.; Lanceros-Méndez, S.; Zhang, Q.; Wang, W. Unveiling Challenges and Opportunities in Silicon-Based All-Solid-State Batteries: Thin-Film Bonding with Mismatch Strain. *Adv. Mater.* **2024**, *36*, 2308590. [CrossRef] [PubMed]
9. He, M.; Fan, Y.; Liu, S.; Wang, S.; Wu, T.; Chen, D.; Hu, A.; Yan, C.; Yan, Y.; Long, J.; et al. The Origin of Li2S2 Reduction Mechanism Modulated by Single-Atom Catalyst for all Solid-State Li-S Batteries. *Adv. Energy Mater.* **2025**, *15*, 2405642. [CrossRef]
10. Yang, S.-J.; Hu, J.-K.; Jiang, F.-N.; Yuan, H.; Park, H.S.; Huang, J.-Q. Safer solid-state lithium metal batteries: Mechanisms and strategies. *InfoMat* **2024**, *6*, e12512. [CrossRef]
11. Zhang, H.; Zhang, Y.; Cao, C.; Zhao, W.; Huang, K.; Zhang, Y.; Shen, Y.; Li, Z.; Huang, Y. Lithium–sulfur pouch cells with 99% capacity retention for 1000 cycles. *Energy Environ. Sci.* **2024**, *17*, 7047–7057. [CrossRef]
12. Pokharel, J.; Cresce, A.; Pant, B.; Yang, M.Y.; Gurung, A.; He, W.; Baniya, A.; Lamsal, B.S.; Yang, Z.; Gent, S.; et al. Manipulating the diffusion energy barrier at the lithium metal electrolyte interface for dendrite-free long-life batteries. *Nat. Commun.* **2024**, *15*, 3085. [CrossRef] [PubMed]

13. Chen, Z.; Wang, X.; Qian, S.; Liang, H.-P.; Chen, M.; Shen, Z. In-situ construction of LiCl-rich artificial solid electrolyte interphase for high-performance lithium metal anode. *ChemSusChem* **2025**, *18*, e202402638. [CrossRef] [PubMed]
14. Jeong, Y.H.; Won, G.; Kim, S.; Jeong, D.; Kwon, D.-S.; Yong, D.K.; Choi, J.; Ahn, H.W.; Kim, S.; Lim, M.; et al. Molecularly engineered artificial solid electrolyte interphase with tailored lithiophilicity and solvent-phobicity for stable lithium metal batteries. *Small* **2025**, *21*, 2411861. [CrossRef] [PubMed]
15. Song, C.; Pan, L.; Wu, J.; Chen, L.; Zhao, H.; Pan, H.; Wu, S.; Yang, L.; Jiang, Y.; Li, Y.; et al. Bioinspired interfacial nanofluidic layer enabling high-rate and dendrite-free lithium metal negative electrodes. *Nat. Commun.* **2025**, *16*, 8056. [CrossRef] [PubMed]
16. Cao, Q.; Fu, D.; He, X.; Huang, Y.; Yao, N.; Song, C.; Song, H.; Wang, C. Uniform fast-kinetic anode/cathode electrolyte interphases enable high-performance 3C Li-metal batteries with >99.9% Coulombic efficiencies. *Nano-Micro Lett.* **2026**, *18*, 243. [CrossRef] [PubMed]
17. Chen, W.; Hu, Y.; Liu, Y.; Wang, S.; Hu, A.; Lei, T.; Li, Y.; Li, P.; Chen, D.; Xia, L.; et al. Ultralong Cycling and Safe Lithium–Sulfur Pouch Cells for Sustainable Energy Storage. *Adv. Mater.* **2024**, *36*, 2312880. [CrossRef] [PubMed]
18. Hu, A.; Chen, W.; Du, X.; Hu, Y.; Lei, T.; Wang, H.; Xue, L.; Li, Y.; Sun, H.; Yan, Y.; et al. An artificial hybrid interphase for an ultrahigh-rate and practical lithium metal anode. *Energy Environ. Sci.* **2021**, *14*, 4115–4124. [CrossRef]
19. Hu, X.; Zhao, Z.; Yang, Y.; Zhang, H.; Lai, G.; Lu, B.; Zhou, P.; Chen, L.; Zhou, J. Bifunctional self-segregated electrolyte realizing high-performance zinc–iodine batteries. *InfoMat* **2024**, *6*, e12620. [CrossRef]
20. Jie, Y.; Wang, S.; Weng, S.; Liu, Y.; Yang, M.; Tang, C.; Li, X.; Zhang, Z.; Zhang, Y.; Chen, Y.; et al. Towards long-life 500 Wh kg−1 lithium metal pouch cells via compact ion-pair aggregate electrolytes. *Nat. Energy* **2024**, *9*, 987–998. [CrossRef]
21. Hu, B.; Zhang, S.; Ning, Z.; Spencer-Jolly, D.; Melvin, D.L.R.; Gao, X.; Perera, J.; Pu, S.D.; Rees, G.J.; Wang, L.; et al. Deflecting lithium dendritic cracks in multi-layered solid electrolytes. *Joule* **2024**, *8*, 2623–2638. [CrossRef]
22. Zhao, L.; Peng, Y.; Dou, P.; Li, Y.; He, T.; Ran, F. Surface chemistry of electrode materials toward improving electrolyte-wettability: A method review. *InfoMat* **2024**, *6*, e12597. [CrossRef]
23. He, Y.; Shi, Z.; Liu, M.; Li, X.; Li, Y.; Zhang, J.; Xu, C.; Qiu, B.; Liu, Z. Optimizing Li plating behavior via controlling areal capacity of a cathode for cycling stability on 600 W h kg−1 lithium-metal batteries. *ACS Appl. Mater. Interfaces* **2024**, *16*, 33475–33484. [CrossRef] [PubMed]
24. Han, G.; Vasylenko, A.; Daniels, L.M.; Collins, C.M.; Corti, L.; Chen, R.; Niu, H.; Manning, T.D.; Antypov, D.; Dyer, M.S.; et al. Superionic lithium transport via multiple coordination environments defined by two-anion packing. *Science* **2024**, *383*, 739–745. [CrossRef] [PubMed]

Disclaimer/Publisher's Note: The statements, opinions and data contained in all publications are solely those of the individual author(s) and contributor(s) and not of MDPI and/or the editor(s). MDPI and/or the editor(s) disclaim responsibility for any injury to people or property resulting from any ideas, methods, instructions or products referred to in the content.